Solar Physics (2006) 234: 115–134
DOI: 10.1007/s11207-006-0047-z © Springer 2006

IMAGING SPECTROSCOPY OF A SOLAR FILAMENT USING A TUNABLE Hα FILTER

JONGCHUL CHAE
Astronomy Program, School of Earth and Environmental Science, Seoul National University, Seoul 151-742, Republic of Korea
(e-mail: chae@astro.snu.ac.kr)

YOUNG-DEUK PARK
Korea Astronomy and Space Science Institute, 61-1, Whaam-Dong, Yooseong-Gu, Daejeon 305-348, Republic of Korea

and

HYUNG-MIN PARK
Korea Astronomy and Space Science Institute, 61-1, Whaam-Dong, Yooseong-Gu, Daejeon 305-348, Republic of Korea; Department of Astronomy and Space Science, Chungnam National University, Daejeon 305-764, Republic of Korea

(Received 15 August 2005; accepted 28 November 2005)

Abstract. Observations using a narrow band Hα filter still remain one of the best ways to investigate the fine structures and internal dynamics of solar filaments. Hα observations, however, have been usually carried out with the peak response of the filter fixed at a single wavelength, usually at the centerline, in which the investigation is limited to the Hα morphology and its time evolution. In this paper, we demonstrate that the Hα spectroscopy that takes Hα images successively at several wavelengths is a useful tool in the study of solar filaments on the solar disk. Our observation of a filament was carried out on August 3, 2004 at Big Bear Solar Observatory using the 10-inch refractor. The Lyot Hα filter was successively tuned to five wavelengths: $-0.6, -0.3, 0.0, +0.3$, and $+0.6$ Å from the Hα line center. Each set of wavelength scan took 15 s. After several steps of data reduction, we have constructed a five-wavelength spectral profile of intensity contrast at every spatial point. The contrast profile at each spatial point inside the filament was reasonably well fit by the cloud model as far as the contrast is high enough, and allowed us to construct the maps of τ_0, v, $\Delta\lambda_D$ and S in the filament. We also found that the line center method that is often used, always yields line-of-sight velocities that are systematically lower than the cloud model fit. Our result suggests that taking Hα images at several wavelengths using a tunable filter provides an effective way of deriving physically meaningful parameters of solar filaments. Particularly constructing the time sequence of v maps appears to be a useful tool for the study of internal dynamics, like counterstreaming, in filaments.

1. Introduction

Hα observations of filaments are commonly performed at a single specified wavelength, usually at the centerline using a very narrow band filter. A time series of Hα monochromatic images of a filament obtained from such observations is used to infer the temporal changes in the morphology and brightness of the filament. When

carefully analyzed, the morphological changes may be exploited to infer not only the transverse motion of the filament as a whole on the plane of sky, but also the velocities of fine structures comprising it. The velocities of filament substructures have been determined using different ways such as manual tracing (Ziker, Engvold, and Martin, 1998; Jing *et al.*, 2003), local correlation tracking (Yi and Molowny-Horas, 1995; Chae *et al.*, 2000) and time-slice diagram (Lin, Engvold, and Wiik, 2003).

It goes without saying that more physical information on filaments can be retrieved from Hα observations at many wavelengths than from single wavelength observations. Multi-wavelength Hα observations are particularly useful in inferring the line-of-sight component of plasma velocity using the Doppler effect. Some people (Martres *et al.*, 1981; Suematsu, Wang, and Zirin, 1995; Lin, Engvold, and Wiik, 2003) used Hα images recorded at two or three wavelengths to infer the line-of-sight velocity, but the limited spectral information requires some assumptions, and the obtained values may systematically deviate from the true ones. To reduce the ambiguity in data interpretation arising from the limited spectral information, Hα data taken at a more number of wavelengths are needed.

A series of studies on the Doppler shifts inside filaments on the disk were carried out (Martres *et al.*, 1981; Simon *et al.*, 1986; Schmieder *et al.*, 1991; Mein, Mein, and Wiik, 1994) based on the Hα observations made with the Multi-Channel Subtractive Double Pass (MSDP) spectrograph (Mein, 1977). The basic output of this instrument is a set of images simultaneously taken at several different, usually around 10 wavelengths. The data are used to construct a line profile by interpolation at every pixel in the field of view. The MSDP spectrograph is a well-designed powerful instrument that can obtain the spectral information and spatial information simultaneously. Its weak feature is that the field of view covered by the instrument is narrow (about $30''$).

The present paper was motivated by the possibility of Hα imaging spectroscopy using a tunable birefringent (Lyot) filter. The principle is simple: to take a series of monochromatic images successively at different wavelengths, namely filter scan. In this kind of filter scan the images taken at different wavelengths are not simultaneous, which may produce a systematic effect in the data interpretation. If, however, the duration for each filter scan is so short that the intrinsic change occurring during the filter scan is negligible, the observations at different wavelengths may be considered to be practically simultaneous.

Whether a filter scan may be considered practically simultaneous or not depends on the number of wavelengths, the camera speed, and the shortest time scale of significant variations in solar features of interest. The time scale of significant change in filaments appears to be longer than 1 min unless they are erupting. In the present paper we have chosen five wavelengths -0.6, -0.3, 0.0, $+0.3$, and $+0.6$ Å from the Hα centerline. We will show that this choice is good enough for the study of structure and dynamics of filaments. Specifically the data taken at the five wavelengths seem to yield reasonable estimates of the four physical

parameters (optical thickness, line-of-sight velocity, Doppler width, and source function) of filaments.

The present paper is mainly devoted to the methods of observation, data reduction, and data analysis with an emphasis put on the effectiveness of the Hα imaging spectroscopy based on the filter scan. More scientific results will be reported in subsequent works.

2. Observations

We have developed an observing system with a fast CCD camera that is to be used mainly at Big Bear Solar Observatory. It consists of a 1024 × 1024 CCD camera (DALSTAR 1M30P) made by the Dalsa Corporation, a frame grabber (PCI-1422) made by the National Instrument, a personal computer, and the Microsoft Visual C++ program. The camera is a 12-bit frame transfer camera with a frame rate of up to 30 fps, and has a pixel size of 12 μm × 12 μm. Its quantum efficiency is about 20% at the Hα wavelength.

The characteristics and performance of this camera was analyzed by Seo, Park, and Chae (2004). The gain was found to be about 43 e^- per DN in the default mode of operation, and about 20 e^- per DN if the camera gain step is set to 2 as we did in our observations. The dark current at the room temperature was estimated to be about 340 e^- s^{-1} per pixel. With the exposure of 60 ms, the contribution of dark current is about 1 DN per pixel, which is smaller than the readout noise 1.3 DN. The bias level was found to be 48.5 DN.

The program we developed controls the camera parameters such as the integration time, binning, frame rate, gain via the RS-232-compatible serial interface, and acquire images using the frame grabber interface. During the data acquisition, the program performs near real-time image processing such as frame integration and frame selection. Moreover, through the communication with the light beam control computer of the observatory, the program can set the pointing of the telescopes and the central wavelength of the Hα filter.

Our Hα observations were carried out from 15:45 UT to 24:00 UT on August 3, 2004 at Big Bear Solar Observatory using the 10-inch refractor equipped with a Zeiss Hα birefringent filter of 0.25 Å bandwidth. One pixel of the camera corresponds to 0.375″ or 270 km on the Sun. The filter was successively tuned to the five wavelengths at Hα −0.6, −0.3, 0.0, +0.3, and +0.6 Å on the basis of a computer control. The exposure time was taken to be 60 ms and the corresponding frame rate was found to be 16 fps. The technique of frame selection was applied and only the best image among 30 frames was saved at each wavelength. It takes one or a few seconds to mechanically switch the central wavelength of the filter from one value to another, with the specific duration depending on the wavelength difference. It took 15 s to finish one scan of five wavelengths and 4 s to resume the next scan. As a result of the observing run, we obtained a total of 7308 images this day. The quiet

Sun averages of data numbers recorded on the CCD camera ranged from 1200 DN (centerline) to 2400 DN (±0.6 Å).

3. Data Processing and Analysis

3.1. Basic image processing

Figure 1 shows an example of a raw Hα image. The image contains several prominent artifacts that should be taken into account in the basic image processing, such as (1) dark edges introduced by the field stop, (2) large-scale nonuniform illumination or vignetting, (3) dust dots existing here and there, (4) faint streaks in the upper left corner, and (5) a localized fringe pattern near the center of the image.

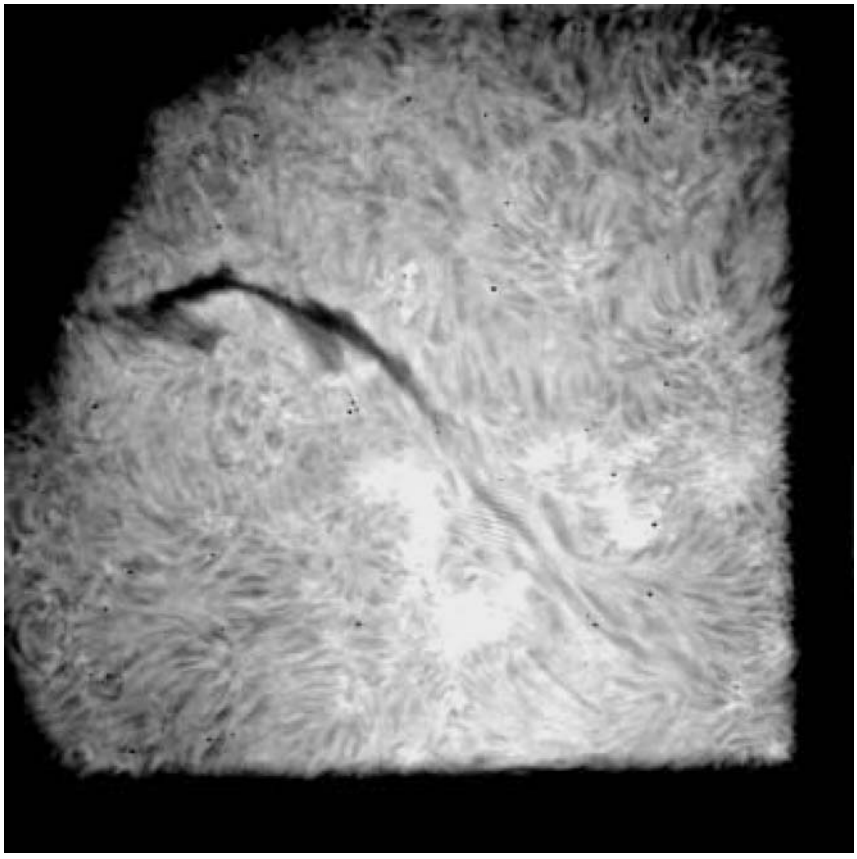

Figure 1. Example of an unprocessed Hα image.

3.1.1. *Masking*

The exclusion of the dark edges are required in the image processing since these regions do not contain enough information and may introduce unexpected errors in image processing. For this purpose we have introduced a mask. A mask is a binary image used to isolate specific features in the original image. The pixels of the features not to be used in image processing are set to zero, and other pixels, to one. We use an Interactive Data Language (IDL) program (cw_defroi.pro) to choose the region of interest which defines the nonzero pixels in the mask.

3.1.2. *Subtraction of bias/dark image*

The correction for the bias and dark current is done straightforward by subtracting the dark frame that is taken with the same exposure as the observations. The left panel of Figure 2 shows such a dark frame. The mean and standard deviation of (bias+dark current) was found to be 49.9 ± 3.3 DN.

3.1.3. *Flat-fielding*

The most critical part of our data reduction is flat-fielding. We make use of Chae's (2004) method which determines the flat pattern from a set of relatively shifted images. Since the flat pattern depends on the wavelength of the filter, a set of shifted images are required at every wavelength. Moreover, since the flat pattern may change with time, it is necessary to take flat calibration images as often as possible. Therefore, performing flat calibration observations requires a careful plan. Fortunately, in Chae's (2004) method the images taken for the flat calibration can be used also for the science, so that the interruption of the main observations is not required for flat observations.

In the present study, we have used an improved version of Chae's algorithm. The improvement is the generalized use of the weight function w in Equation (4)

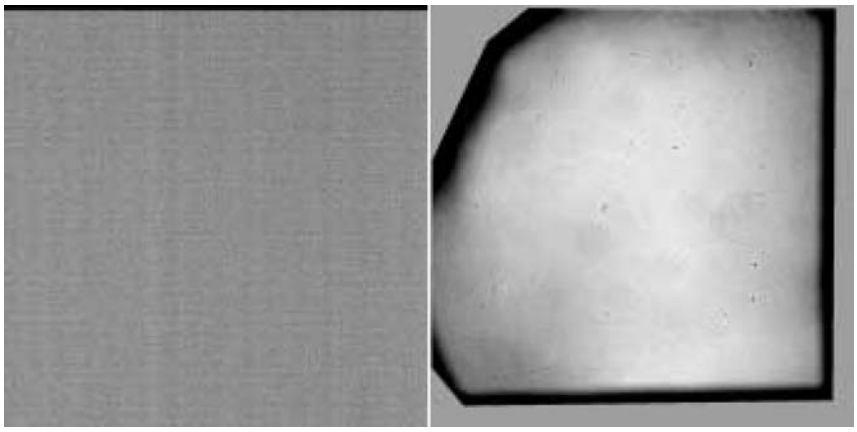

Figure 2. Examples of a dark frame (*left*) and a flat pattern (*right*).

of Chae (2004). It was originally introduced to deal with the boundary effects. It was set to zero at the pixels which, when shifted by some amounts, lie outside the boundary. In the new version, w also incorporates the mask we defined above. It is also set to zero at pixels where the mask is zero.

The right panel of Figure 2 shows an example of the flat pattern we obtained. The polygon represents the mask we used. Outside the polygon, the flat pattern is set to unity for display convenience. In this image, we find all the prominent artifacts seen in Figure 1 such as vignetting, dust dots, streaks, and fringe. In addition to these, we also see fainter artifacts that are not clear in Figure 1.

3.1.4. *Dealing with nonperfect flat-fielding*

If the flat pattern is well determined, and it does not change with time, the artifacts in a raw image are completely removed by dividing it by the flat pattern. However, we found that two kinds of artifact patterns were not completely removed.

One is dust dots. In some images, they were completely removed, and in other images they were not. We discovered that all of the dust dots as a whole moved across the detector pixels slightly from time to time. The amount of displacement was about one pixel. We do not understand how this offset variation happens, but it is likely that the offset is related to some anomaly in the data transfer of the CCD camera. Unless this offset variation is properly taken into account, the dust dots are not completely removed even after the conventional flat-fielding because they have sharp intensity gradients. We solved this problem by correcting for this offset variation before we obtain the flat pattern and apply the flat-fielding. We determined the relative offset of dust dots in every image by comparing a small subimage containing a few prominent dots with that of a reference frame, and then displaced the image back by the same offset.

The other is the fringe pattern. This artifact is hardly completely removed by the flat fielding since it changes with time. Therefore after the flat-fielding, we apply additional image processing to remove this pattern. The fringe pattern seen in a raw image appears as two small dots with high power in its Fourier transform. We define two small spectral areas encircling these Fourier dots, and suppress the power at these areas to zero. The inverse Fourier transform yields a new image in which the fringe pattern is removed.

Figure 3 shows the processed image that was obtained by applying the basic image processing.

3.2. CONSTRUCTING CONTRAST DATA CUBE

Many chromospheric features observed in the Hα line appear darker than the surrounding since they scatter off some of the Hα radiation incident from below. For the description of the effect of a chromospheric feature on the Hα radiation, it is useful to introduce the contrast $C_\lambda(x, y)$ between the intensity of radiation emergent out of the feature, $I_\lambda(x, y)$ and the intensity of radiation incident into the feature from

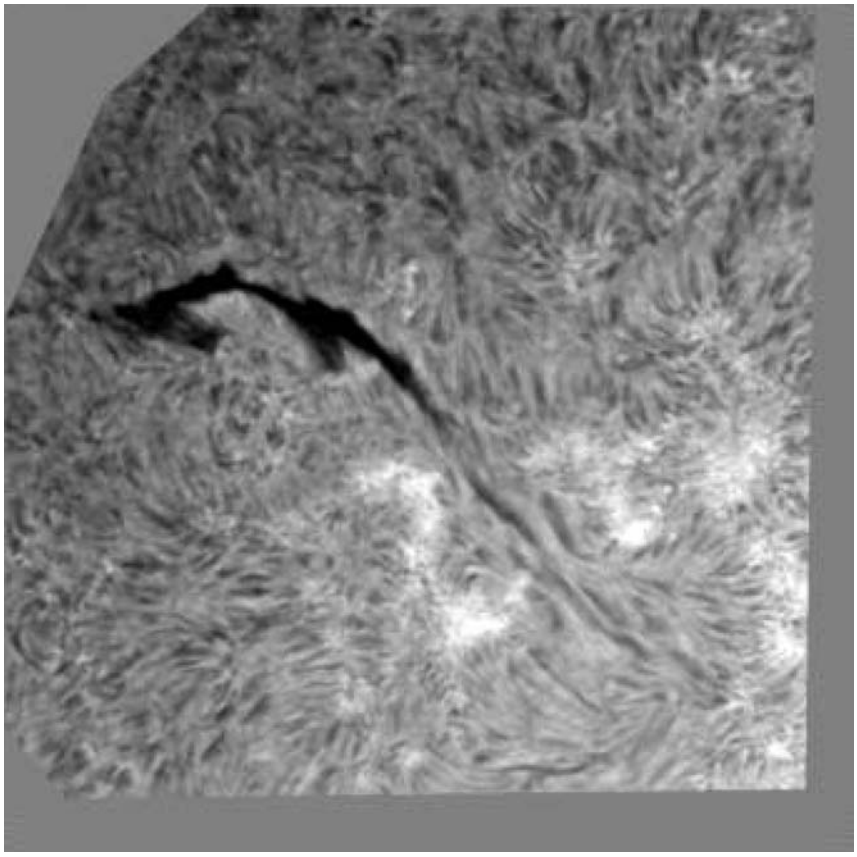

Figure 3. Example of a processed Hα image.

below, $I_{\lambda,0}(x, y)$

$$C_\lambda(x, y) \equiv \frac{I_\lambda(x, y) - I_{\lambda,0}(x, y)}{I_{\lambda,0}(x, y)} \tag{1}$$

where λ is the wavelength and (x, y) is the position of the feature on the image plane. To a good approximation, we may set $I_{\lambda,0}(x, y)$ equal to the intensity of the radiation from the neighborhood without any other chromospheric features. From the observational viewpoint, working on the contrast is more convenient than working on the intensity itself because observed contrast depends on the difference and ratio of the two observed intensities so that it may be little subject to problem of absolute intensity calibration.

Our task is then to construct a four-dimensional array for the contrast data C that depend on position (x, y), wavelength λ, and time t. This task was done in several steps: (1) defining $I_{\lambda,0}$ and calculating C for every image, (2) image registration, and (3) additional image processing.

3.2.1. *Calculation of contrast*
We determine the contrast $C^{\rm obs}_{\lambda,0}(x, y)$ from observations in two steps. Firstly, we apply a low order polynomial surface fit to the observed intensity image $I^{\rm obs}_{\lambda}(x, y)$ over the field of view to obtain the rough estimates of the reference intensity which we denote by $I'_{\lambda}(x, y)$, and the first estimate of the contrast.

$$C'_{\lambda}(x, y) \equiv \frac{I^{\rm obs}_{\lambda}(x, y) - I'_{\lambda}(x, y)}{I'_{\lambda}(x, y)}. \tag{2}$$

The reference intensity $I'_{\lambda}(x, y)$ obtained in this way, however, is not precisely representing $I_{\lambda,0}(x, y)$, the intensity of the radiation from the neighborhood without any chromospheric feature, since the surface fit has included the contribution of many chromospheric features in the field of view. The correction for this subtle discrepancy can be made as follows. We first choose a specific chromospheric feature of our interest – the filament itself in the present study, and then select a number of data pixels which surround this feature and are free from other chromospheric features. These pixels define our local reference area. We take the average of contrast over these reference pixels, $\langle C'_{\lambda}\rangle_{\rm R}$. The corrected contrast is obtained from the relation

$$C^{\rm obs}_{\lambda}(x, y) = \frac{C'_{\lambda}(x, y) - \langle C'_{\lambda}\rangle_{\rm R}}{1 + \langle C'_{\lambda}\rangle_{\rm R}} \tag{3}$$

and the corrected reference intensity is given by

$$I^{\rm obs}_{\lambda,0}(x, y) = I'_{\lambda}(x, y)\,(1 + \langle C'_{\lambda}\rangle_{\rm R}). \tag{4}$$

3.2.2. *Data registration*
We use a total of 128 successive contrast images taken at the same wavelength for about 40 min to construct a cube of three-dimensional data. The image taken in the middle of the sequence serves as a reference. All the images are compared to this reference image and their relative displacements are determined. The relative displacement between an image and the reference image is determined by maximizing the cross-correlation of the two images. We find that cross-correlating subimages often better works than doing the whole images especially when vignetting is serious. All the images are then shifted back by the amount of relative displacements determined in this way. This completes the construction of a three-dimensional data cube. This process is repeated for every set of images taken at different wavelengths.

3.2.3. *Aligning different wavelengths*
A complete set of data cubes that can be used for imaging spectroscopy is obtained by aligning the five data cubes constructed from images taken at the five different wavelengths during the same observing run. The alignment of all the images requires the knowledge of the relative displacements among different wavelengths. We compare the five images taken at the five wavelengths in the middle of the

observing run. Specially we determine the relative displacements of the four reference images taken at the four wavelengths other than the line center with respect to the Hα centerline reference image. Since the morphology of Hα features varies with the wavelength, the comparison for the determination of relative displacement is made successively between two adjacent wavelengths. That is, the Hα−0.6 Å image is compared with the Hα−0.3 Å image, and the Hα−0.3 Å image, with the Hα centerline image. In the same way, Hα+0.6 Å image is compared with Hα+0.3 Å image, and Hα + 0.3 Å image, with the Hα centerline image.

3.3. Additional image processing

3.3.1. *Image enhancement*

The contrast image is enhanced using the maximum entropy image deconvolution (Chae *et al.*, 1998b). This is to correct for the blurring effect of the seeing. We adopt a point spread function of the form empirically found by Chae *et al.* (1998a) with its full width at half maximum (FWHM) set to two detector pixels. The true FWHM of the point spread function should be equal to or greater than two pixels. Therefore, our deconvolution undercorrects the blurring. It is a conservative image enhancement leaving little worry about artifacts that are often introduced in image deconvolution. Note that image enhancement may be applied either before or after the data cube is constructed. In fact, we applied it before the construction of the data cube since the higher contrast in the enhanced images will be helpful in cross-correlating images.

3.3.2. *Subsonic filtering*

A subsonic filter proposed by Title *et al.* (1989) is applied to each time sequence of contrast images. This filtering is effective in suppressing the noise in the data as well as oscillations. The important parameter in the subsonic filter is the cutoff speed. A smaller value it has, stronger is the suppression of oscillations and noise. We choose 35 km s^{-1} for it. The transverse motion inside a quiescent prominence is normally much smaller than this value. If one is much interested in the oscillations and waves that have high phase speeds, one should be careful in applying this filtering.

3.4. Wavelength calibration and photometric accuracy

3.4.1. *Wavelength calibration*

A wavelength set by the instrument λ_{inst} may be a little different from the true wavelength λ_{true} either because the instrumental wavelength setting is not precise or because the whole area of the observed region in the field of view is Doppler shifted. Let's introduce the relative offset $\delta\lambda$ defined by the equation

$$\lambda_{\text{true}} = \lambda_{\text{inst}} + \delta\lambda \tag{5}$$

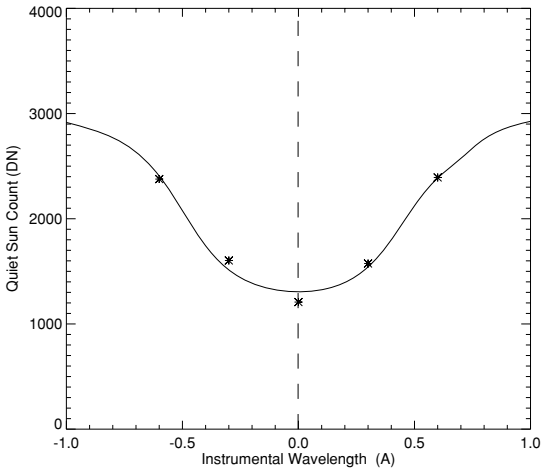

Figure 4. Model intensity profile fit to the quiet Sun intensity data obtained from the five wavelength filtergrams.

where $\lambda_{\rm true}$ and $\lambda_{\rm inst}$ are the wavelengths measured from the Hα line center. A reference is required to determine $\delta\lambda$. We set a reference to the center of the line profile constructed by the spatial averages of $I^{\rm obs}_{\lambda,0}(x, y)$ in Equation (4). We determine the instrumental wavelength of the center of this reference line profile $\lambda^{\rm ref}_{\rm inst}$ by applying a model profile fit to data at the five wavelengths

$$\left\langle I^{\rm obs}_{\lambda_{\rm inst},0}\right\rangle = a\, I^{\rm mod}\left(\lambda_{\rm inst} - \lambda^{\rm ref}_{\rm inst}\right) + b \tag{6}$$

with the three free parameters a, $\lambda^{\rm ref}_{\rm inst}$, and b. Here the bracket refers to the average of the intensity over the nearby quiet Sun. We set the model profile $I^{\rm mod}$ equal to the Hα disk-center intensity profile in Wallace, Hinkle, and Livingston (1998).

The offset is then given by $\delta\lambda = -\lambda^{\rm ref}_{\rm inst}$ and the wavelength calibration is done based on the expression

$$\lambda_{\rm true} = \lambda_{\rm inst} - \lambda^{\rm ref}_{\rm inst}. \tag{7}$$

The value of $\lambda^{\rm ref}_{\rm inst}$ may vary depending on the condition of the instrument and the observing region, but it is usually much smaller than the bandwidth of the filter.

Figure 4 represents the Hα line profile constructed from the filtergrams and the result of the model fit in Equation(6). The line center is found to be at the instrumental wavelength 0.003 Å. This difference is negligibly small, and therefore the calibrated wavelengths in these images are practically the same as the instrumental wavelengths.

3.4.2. *Photometric accuracy*

A conservative estimate of the noise in the contrast data can be obtained from the difference between two frames successively taken. The standard deviation in the

contrast data we produced is found to be around 0.015 at all the wavelengths. This value is in fact the upper bound for the noise since it also includes the effect of intrinsic temporal variations occurring between the two frames.

3.5. CLOUD MODEL FITTING

A single set of our data to be analyzed is a four-dimensional array $C_\lambda(x, y, t)$ that represents the variation of contrast C with the wavelength λ, the observing direction (x, y), and the observing time t. The grid parameters are $\Delta\lambda = 0.3$ Å, $\Delta x = \Delta y = 0.375''$, and $\Delta t = 20$ s.

For data analysis we adopt the so-called cloud model introduced by Beckers (1964). It describes the contrast between the intensity of radiation emerging out of a cloud I_λ^{out}, and the intensity radiation incident from below into the cloud I_λ^{in}, in terms of the four model parameters S, τ_0, λ_c, and $\Delta\lambda_D$ like

$$C_\lambda^{\text{mod}} \equiv \frac{I_\lambda^{\text{out}} - I_\lambda^{\text{in}}}{I_\lambda^{\text{in}}} = \left(\frac{S}{I_\lambda^{\text{in}}} - 1\right)(1 - \exp(-\tau_\lambda)) \tag{8}$$

with

$$\tau_\lambda = \tau_0 \exp\left(-\left(\frac{\lambda - \lambda_c}{\Delta\lambda_D}\right)^2\right). \tag{9}$$

The model requires the knowledge of I_λ^{in}. For simplicity we neglect its dependence on the location on the disk and set it equal to the Hα disk-center intensity profile in Wallace, Hinkle, and Livingston (1998). The source function S is assumed to be independent of the wavelength, which is likely when the scattered radiation is completely redistributed over the line profile.

The four parameters of the cloud model S, τ_0, λ_c, and $\Delta\lambda_D$ to be determined are related to physical quantities such as line-of-sight velocity, kinetic temperature, nonthermal motion, hydrogen density, geometrical thickness, and so on. Inferring these quantities from the model parameters, however, is not an easy task, and definitely requires more knowledge on the non-LTE radiative transfer inside filaments. So we do not intend to infer the physical parameters except the line-of-sight velocity which is directly calculated from λ_c.

In this regard, it is worthwhile to mention the non-LTE inversion procedure introduced by Molowny-Horas *et al.* (1999). They regarded four physical quantities (temperature, electron density, nonthermal motion, bulk motion, and geometrical thickness) as the free parameters to be determined from the model fits. The fitting was performed using a large grid of models preconstructed by means of a multilevel non-LTE transfer code. We think the non-LTE inversion procedure is useful in determining temperature and density, whereas the cloud model is effective in determining line-of-sight velocity.

We use a constrained nonlinear square fitting technique Chae, Yun, and Poland (1998) introduced, to fit the data by the cloud model. The basic idea of this technique is to provide the expectation values of the free parameters and their standard deviations from the true values as well as the data to be fit. The method seeks a set of free parameters $\boldsymbol{p} = (p_0, p_1, \ldots, p_{N-1}) = (S, \tau_o, \lambda_c, \Delta\lambda_D)$ that minimizes the sum H of the data χ^2 and the expectation χ^2,

$$H(\boldsymbol{p}) = \sum_{j=0}^{M-1} \left(\frac{C_j^{\rm obs} - C_j^{\rm mod}(\boldsymbol{p})}{\sigma_j} \right)^2 + \sum_{i=0}^{N-1} \left(\frac{p_i - p_i^e}{\epsilon_i} \right)^2 . \tag{10}$$

The latter expectation term plays a role of regularizing the solution by constraining the probable range of the free parameters. If one uses very small values for ϵ_i, the solution gets very close to the set of expectation values p_i^e, without being much constrained by the data. On the contrary, if too big values of ϵ_i are used, the solution is mostly constrained by the data, and little by the given expectation values.

After some experience, we have found that unreasonable solutions obtained from the fit to the data only are characterized by either too large or too small values of $\Delta\lambda_D$. Hence, an effective way of constraining fitting without introducing significant bias is to constrain the width $\Delta\lambda_D$ only. The expectation value of $\Delta\lambda_D$ and its corresponding value of ϵ adopted in the present study are 0.5 Å and 0.3 Å, respectively. We set ϵ to infinitely large values for the free parameters other than $\Delta\lambda_D$, not to constrain them. The noise in the data is $\sigma_j = 0.015$. We will discuss the effect of the constrained fitting later.

4. Results

4.1. CONTRAST IMAGES

Figure 5 presents one example of calibrated contrast images. They show only a region enclosing the filament of our interest, with a field of view $169'' \times 94''$. As is well known the filament is better visible at the bands near the centerline than at the off-bands. We found that the contrast is a little higher at ± 0.3 Å than at the centerline.

This filament has two well-defined barbs. Their magnetic structure was already studied by Chae *et al.* (2005), who found that the termination of these barbs occurred above the minor polarity inversion line, not on magnetic elements of minor polarity. A careful examination of the images may reveal that the filament including these barbs is made up of many fine threads.

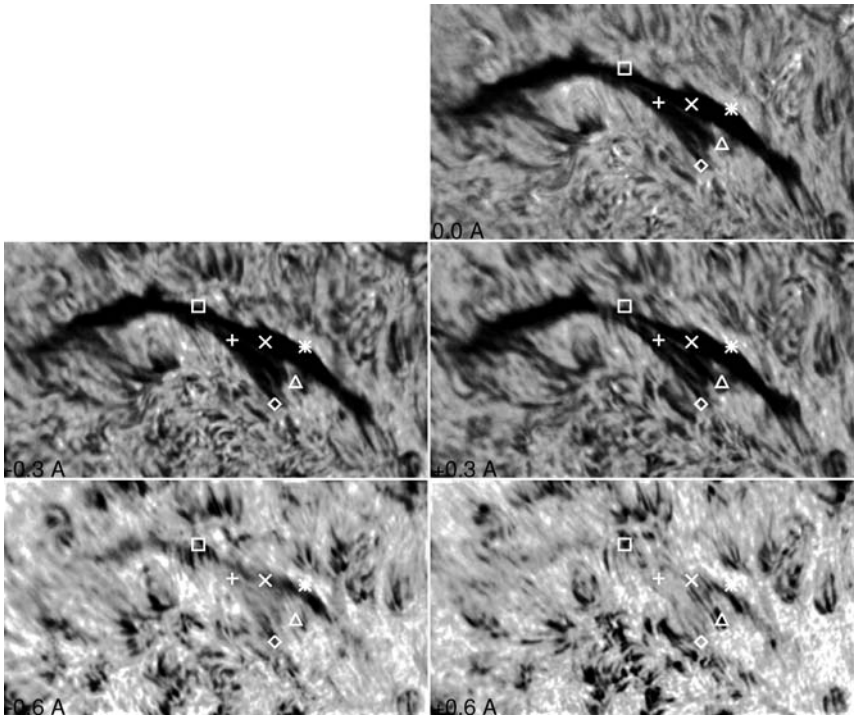

Figure 5. A set of contrast images constructed at the wavelengths of −0.6, −0.3, 0, +0.3, and +0.6 Å. The *symbols* mark the points at which the contrast profiles are examined in detail.

4.2. CLOUD MODEL FIT: EXAMPLES

Figure 6 shows the contrast profiles constructed at six selected points in the filament. These points are marked in symbols in Figure 5. These contrast profiles $C_\lambda^{\rm obs}$ were fit by the cloud model specified in Equations (8–9), either with or without the constraint in $\Delta\lambda_{\rm D}$. Figure 6 also shows the corresponding optical thickness profiles as defined by Equation (9).

The first two points represent the points that are in the interior of the filament and are dark enough. The profiles at these points are fairly well fitted by the cloud model. The first profile was taken from a very dark point (×) inside the filament that may represent the spine of the filament. It has contrast as high as 0.4, and the peak optical thickness τ_0 as large as 1.8. The profile is slightly blue-shifted with a corresponding line-of-sight velocity of $-1.0\,{\rm km\,s^{-1}}$. Its width $\Delta\lambda_{\rm D}$ is 0.38 Å. The second profile (+) was taken from another point inside the filament. This point is less dark, but is much better fitted by the cloud model than the first point. Note that there is no significant difference between the constrained fitting and the unconstrained fitting at these points.

The two kinds of fitting produce different results at the third point (∗) that represents the edge of the filament and has low contrast, being barely visible. Both

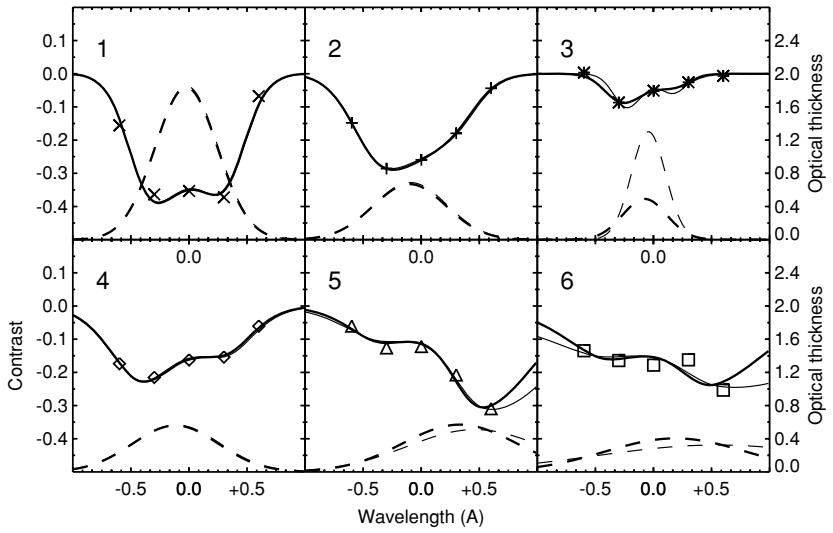

Figure 6. Observed contrast profiles (*symbols*) at the selected positions, and their model fits (*solid curves*). The error bars of the measured profiles are of about the same size as the height of the symbols. The thick solid curves are from the constrained fit, and the thin curves from the unconstrained fit. The thick and thin *dashed curves* are the optical thickness profiles obtained as a result of constrained model fits and unconstrained model fits.

the methods fit the data well, but their results are different. The unconstrained fitting produces a very narrow optical thickness profile ($\Delta\lambda_D = 0.21$ Å) with a peak thickness as large as 1.3, while the constrained fitting does a broader profile ($\Delta\lambda_D = 0.25$ Å) with a smaller peak thickness of about 0.6. We think that the result of the constrained fitting is more reasonable than the other in this case.

The fourth ($\diamond$) and fifth ($\triangle$) points represent the barbs of the filament. In the case of the fourth point, there is no difference between the constrained fitting and unconstrained fitting to the fourth profile ($\diamond$), which is because the data are good enough to well constrain the parameters. The line-of-sight velocity at this point was found to be $-5.3\,\mathrm{km\,s^{-1}}$ (blueshift), indicating that the barb around this point is dynamic. The barb at the other point ($\triangle$) is found to be even more dynamic. Because the absorption is highly redshifted, it appears that the selected wavelengths are not enough to fully cover the redshifted optical thickness profile. As a consequence, the data are not complete enough to constrain the free parameters of the model, and there arises a difference between the constrained model fit and the unconstrained model fit. We find that the constrained fit yields smaller values of width ($\Delta\lambda_D = 0.53$ Å) and Dopplershift ($17\,\mathrm{km\,s^{-1}}$) than the unconstrained fit does in which case we have 0.74 Å and $21\,\mathrm{km\,s^{-1}}$, respectively. Both the models fit the data equally well, but we think that the values from the constrained fit are more conservative estimates.

The last profile ($\square$) illustrates an example in which neither of the constrained fit and the unconstrained fit is satisfactory, even though the constrained fit seems

to produced more reasonable results than the other fit. The region around this point is characterized by the line-of-sight overlap of the filament and the underlying network fibrils as is clear from Figure 5. Therefore the badness of the fit may be attributed to the failure of removing the contribution of the network fibrils.

4.3. MAPS AND DISTRIBUTIONS OF MODEL PARAMETERS

Our further examination of the contrast profile at more number of spatial points in addition to these six contrast profiles has revealed that the spectral parameters sensitively depend on the selected point, varying from point to point at small scales. This characteristic may be understood if the filament consists of numerous fine threads and each thread is in a dynamic state more or less independent of neighboring threads. In this sense, constructing the high resolution maps of spectral parameters appears to be very useful for the study of internal structure and dynamics of a filament.

Figure 7 shows such maps. The optical thickness map in Figure 7 looks similar to the contrast image at the centerline (see Figure 5). The difference in the details between the two may be attributed to the fact that the centerline image is affected by Doppler shift while the optical thickness map is not. The spatial resolution of the optical thickness map appears a little worse than the contrast images. This is because the optical thickness map was constructed from several contrast images taken at slightly different times so that it may be more subject to the seeing than a single contrast image. Nevertheless, the optical thickness map clearly reveals some threads inside the filament.

More structures are visible in the line-of-sight velocity map. Particularly interesting is the existence of closely interlaced velocity structures that are oppositely directed. This may represent the counterstreaming. The line-of-sight velocity in the map ranges from -15 to $15\,\mathrm{km\,s^{-1}}$ with the standard deviation being about $4\,\mathrm{km\,s^{-1}}$. With the geometric projection effect being taken into account, these values are in rough agreement with the reported speeds of the counterstreaming: 5–$20\,\mathrm{km\,s^{-1}}$ reported by Ziker, Engvold, and Martin (1998) and $8\,\mathrm{km\,s^{-1}}$ reported by Lin, Engvold, and Wiik (2003). The detailed analysis of this kind of velocity pattern will shed light on the physical nature of the counterstreaming. This will be the topic of our forthcoming works.

The Doppler width map shows that the interior of the filament has small widths, but surrounding chromospheric network areas have bigger widths. Therefore, the width map appears very useful in identifying filament areas contaminated by the network features.

To examine the effect of image enhancement described in the previous section, we have shown in Figure 8 two kinds of line-of-sight velocity maps constructed from data with and without image enhancement applied, respectively. The two maps are

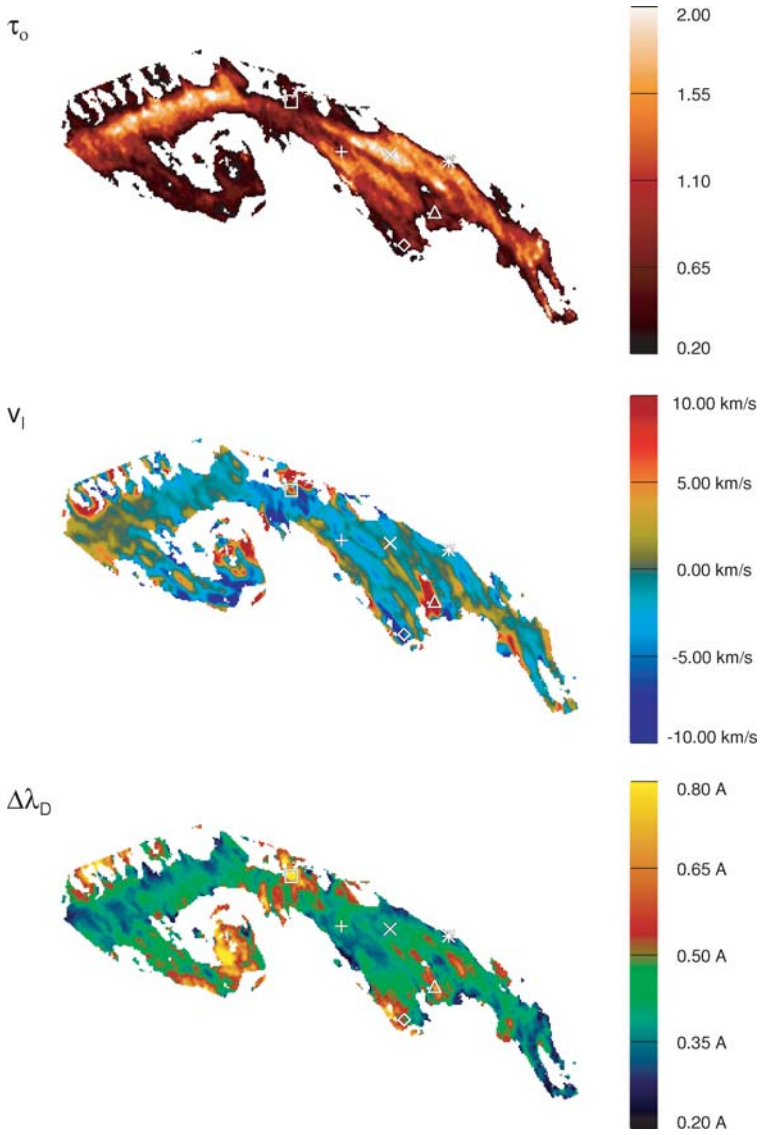

Figure 7. Maps of optical thickness, line-of-sight velocity, and Doppler width from top to bottom. The display of parameters at pixels with $\tau_0 < 0.2$ were suppressed (as the *white color*) for clarity.

very similar, but, as expected, the map with image enhancement is superior to the other in presenting the fine details of the velocity field such as the counterstreaming.

Figure 9 shows the number distributions of the parameters obtained from the cloud model fit. The mean values and standards deviations of the distributions are $\tau_0 = 0.83 \pm 0.47$, $v_l = -0.61 \pm 4.05\,\mathrm{km\,s^{-1}}$, $\Delta\lambda_D = 0.43 \pm 0.11$ Å, and $S = 0.10 \pm 0.03$, respectively.

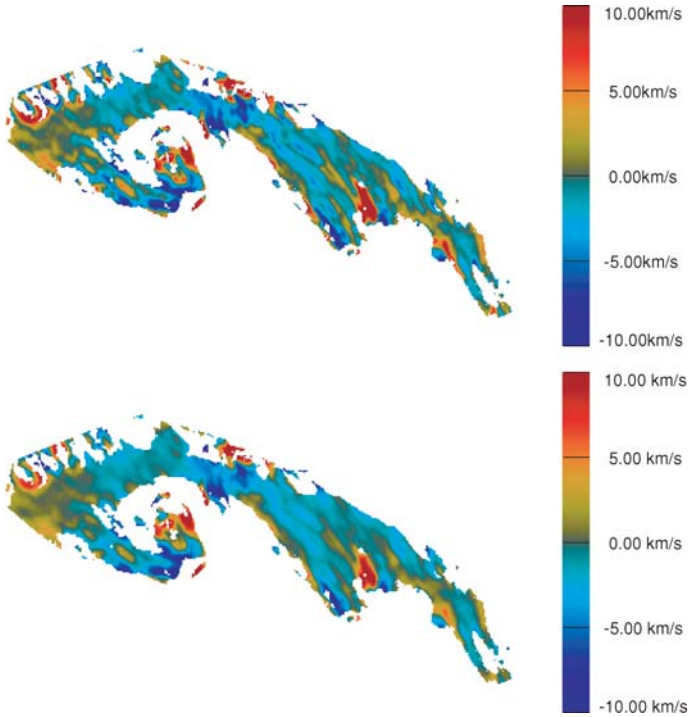

Figure 8. Comparison of line-of-sight velocity maps constructed from data with (*upper*) and without (*lower*) image enhancement applied, respectively.

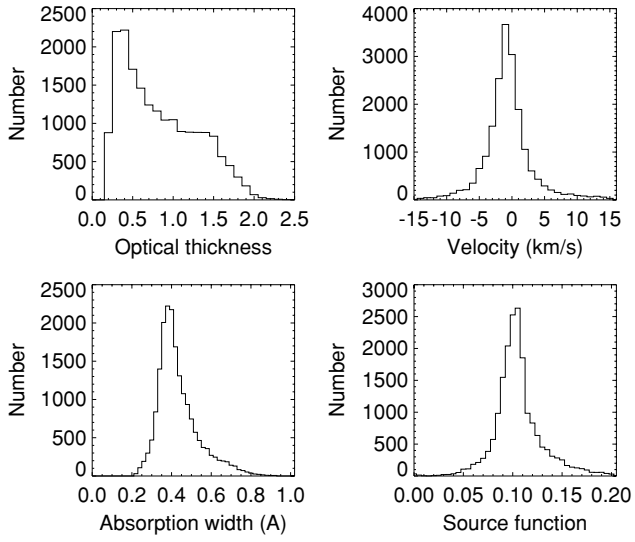

Figure 9. Number distributions of optical thickness, line-of-sight velocity, absorption width, and source function in the filament. Pixels with $\tau_0 < 0.2$ were excluded in these distributions.

4.4. CLOUD MODEL METHOD VS. LINE CENTER METHOD

It would be interesting to compare line-of-sight velocities determined using different methods. We use the cloud model fit to determine the line-of-sight velocity. In this method, the determined velocity represents that of a cloud that absorbs (or precisely speaking scatters) the Hα incident from the photosphere and chromosphere. Another method that is often used is the line center method (e.g., Lin, 2004) that uses the wavelength of the Hα line center to determine the line-of-sight velocity. Figure 10 shows the comparison between the two methods. It is obvious from the figure that the line center method produces smaller values of line-of-sight velocity than the cloud model fit method. Note that the standard deviation of line-of-sight velocities determined from the line center is only $0.9\,\mathrm{km\,s^{-1}}$, much smaller than that in the cloud model fit method by a factor of about 4. The line center velocity is roughly proportional to the cloud model velocity, but the linearity breaks if the cloud model velocity is bigger than $5\,\mathrm{km\,s^{-1}}$. The magnitude of the line center velocity is less than $3\,\mathrm{km\,s^{-1}}$, irrespective of the cloud model velocity.

This big difference between the two methods comes from the fact that the scattering of the incident light by the filament does not alter the Hα line profile much. The line-of-sight velocity determined from the line center may be interpreted as a weighted average of the line-of-sight velocity of the underlying atmosphere (that

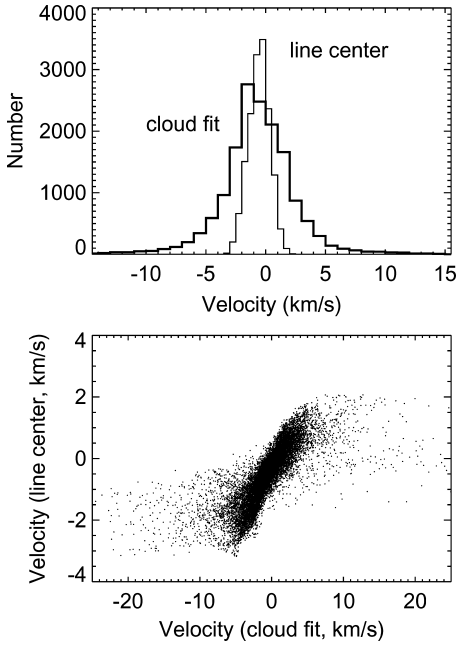

Figure 10. Comparison of line-of-sight velocities between the cloud model fit method and the line center method.

is defined to be zero) and that of the filament (that may not be zero). The weight of the underlying atmosphere is usually bigger than that of the filament, especially at regions with small optical thickness. Therefore, the line-of-sight velocity determined from the line center is always less than the filament velocity. The conclusion obtained for the line center method is equally applied to the chord center method that measures the Doppler shift from the center of the chord with a specified length $\Delta\lambda$ which connects two equidensity points in the line profile, as was already shown by Schmieder *et al*. (1991).

5. Summary and Conclusion

We have taken a sequence of Hα images of a solar filament with the center of the Lyot filter of 0.25 Å bandwidth being successively tuned to the five wavelengths: -0.6, -0.3, 0.0, $+0.3$, and $+0.6$ Å. These data were used to construct five-wavelength contrast spectral profiles at arbitrary spatial points inside the field of view. The contrast profiles at points inside the filament were fit by the cloud model with $\Delta\lambda_D$ being constrained. Our results are summarized as follows:

1. Subsonic filtering is effective in suppressing noise and hence constructing decent maps of parameters, and image enhancement is effective in revealing fine details of the velocity structure in the filament.
2. At points inside the filament that are dark enough and have small line-of-sight velocities, the observed contrast profiles are fairly well fit by the cloud model and there is no difference between the unconstrained fit and the constrained fit.
3. At points either with large line-of-sight velocities or with too small contrast, the constrained fit yields more reasonable fit than the unconstrained fit.
4. At some points where the underlying network features seriously contaminate the filament, the cloud model fit is not good.
5. The cloud model fit yields much more reasonable estimate of line-of-sight velocity of the filament than the line center method and the cord center methods do.

These results are encouraging since the maps of optical thickness, Doppler width, and line-of-sight velocity and their time sequences to be obtained in our approach will provide much more useful physical information on filaments than a time series of Hα images taken at a single wavelength. In the forthcoming works we will investigate the structure and dynamics of filaments using these maps in detail.

Acknowledgements

We would like to thank John Varsik, Sergey Shumko, Alla Shumko, and Randy Fear for their kind assistance in the observations. We greatly appreciate the referee's

comments that helped much in improving the manuscript. This work was supported by the Korea Research Foundation Grant (KRF-2002-015-CS0020).

References

Beckers, J. M.: 1964, Ph.D. thesis, University of Utrecht.
Chae, J.: 2004, *Solar Phys.* **221**, 1.
Chae, J., Moon, Y.-J., and Park, Y.-D.: 2005, *Astrophys. J.* **626**, 574.
Chae, J., Yun, H. S., and Poland, A. I.: 1998, *Astrophys. J. Suppl.* **114**, 151 .
Chae, J., Yun, H. S., Sakurai, T., and Ichimoto, K.: 1998a, *Solar Phys.* **183**, 229.
Chae, J., Yun, H. S., Sakurai, T., and Ichimoto, K.: 1998b, *Solar Phys.* **183**, 245.
Chae, J., Denker, C., Spirock, T. J., Wang, H., and Goode, P. R.: 2000, *Solar Phys.* **195**, 333.
Jing, J., Lee, J., Spirock, T. J., Xu, Y., Wang, H., and Choe, G. S.: 2003, *Astrophys. J. Lett.* **584**, L103.
Lin, Y.: 2004, PhD thesis, University of Oslo.
Lin, Y., Engvold, O. R., and Wiik, J. E.: 2003, *Solar Phys.* **216**, 109.
Martres, M.-J., Mein, P., Schmieder, B., and Soru-Escaut, I.: 1981, *Solar Phys.* **69**, 301.
Mein, P.: 1977, *Solar Phys.* **54**, 45.
Mein, N., Mein, P., and Wiik, J. E.: 1994, *Solar Phys.* **151**, 75.
Molowny-Horas, R., Heinzel, P., Mein, P., and Mein, N.: 1999, *Astron. Astrophys.* **345**, 618.
Schmieder, B., Raadu, M. A., and Wiik, J. E.: 1991, *Astron. Astrophys.* **252**, 353.
Seo, Y.-M., Park, K.-W., and Chae, J.: 2004, *J. Korean Astron. Soc.* **37**, 185.
Simon, G., Schmieder, B., Démoulin, P., and Poland, A. I.: 1986, *Astron. Astrophys.* **166**, 319.
Suematsu, Y., Wang, H., and Zirin, H.: 1995, *Astrophys. J.* **450**, 411.
Title, A. M., Topka, K. P., Ferguson, S. H., Shine, R. A., and SOUP Team: 1989, *Astrophys. J.* **336**, 475.
Wallace, L., Hinkle, K., and Livingston, W.: 1998, *An Atlas of the Spectrum of the Solar Photosphere from 3570 to 7405 Å*, National Solar Observatory, Tucson, Arizona, USA.
Yi, Z. and Molowny-Horas, R.: 1995, *Astron. Astrophys.* **295**, 199.
Zhang, Q. Z., Livingston, W. C., Hu, J., and Fang, C.: 1987, *Solar Phys.* **114**, 245.
Ziker, J. B., Engvold, O., and Martin, S. F.: 1998, *Nature* **396**, 440.